Size-Tunable, Hexagonal Plate-like Cu_3P and Janus-like $Cu-Cu_3P$ Nanocrystals

Luca De Trizio,[†,‡] Albert Figuerola,[†,¶,*] Liberato Manna,[†] Alessandro Genovese,[†] Chandramohan George,[†] Rosaria Brescia,[†] Zineb Saghi,[§] Roberto Simonutti,[‡] Marijn Van Huis,[⊥,∥] and Andrea Falqui[†,*]

[†]Istituto Italiano di Tecnologia, Via Morego 30, 16130 Genova, Italy, [‡]Department of Materials Science, University of Milano Bicocca, Via Cozzi 53, 20125 Milano, Italy, [§]Department of Materials Science and Metallurgy, University of Cambridge, Pembroke Street, Cambridge CB2 3QZ, United Kingdom, [⊥]Kavli Institute of Nanoscience, Delft University of Technology, Lorentzweg 1, 2628 CJ Delft, The Netherlands, [∥]EMAT, University of Antwerp, Groenenborgerlaan 171, 2020 Antwerp, Belgium, and [¶]Departament de Química Inorgànica, Universitat de Barcelona, Martí i Franqués 1-11, 08028 Barcelona, Spain

ABSTRACT We describe two synthesis approaches to colloidal Cu_3P nanocrystals using trioctylphosphine (TOP) as phosphorus precursor. One approach is based on the homogeneous nucleation of small Cu_3P nanocrystals with hexagonal plate-like morphology and with sizes that can be tuned from 5 to 50 nm depending on the reaction time. In the other approach, metallic Cu nanocrystals are nucleated first and then they are progressively phosphorized to Cu_3P. In this case, intermediate Janus-like dimeric nanoparticles can be isolated, which are made of two domains of different materials, Cu and Cu_3P, sharing a flat epitaxial interface. The Janus-like nanoparticles can be transformed back to single-crystalline copper particles if they are annealed at high temperature under high vacuum conditions, which makes them an interesting source of phosphorus. The features of the $Cu-Cu_3P$ Janus-like nanoparticles are compared with those of the striped microstructure discovered more than two decades ago in the rapidly quenched $Cu-Cu_3P$ eutectic of the Cu—P alloy, suggesting that other alloy/eutectic systems that display similar behavior might give origin to nanostructures with flat, epitaxial interface between domains of two diverse materials. Finally, the electrochemical properties of the copper phosphide plates are studied, and they are found to be capable of undergoing lithiation/delithiation through a displacement reaction, while the Janus-like $Cu-Cu_3P$ particles do not display an electrochemical behavior that would make them suitable for applications in batteries.

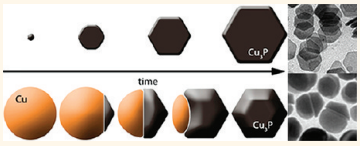

KEYWORDS: nanoparticles · Janus-like particles · copper phosphide · transmission electron microscopy · electron tomography · electrochemical lithiation properties

Transition metal phosphides have attracted much interest in the recent years for their potential in magnetic recording media, catalysis, and as anode materials in lithium ion batteries.[1,2] Especially in batteries, nanostructuration of the active material in the electrodes can introduce improvements with respect to bulk materials in terms of charge/discharge cycling and rates.[3−6] Several efforts have been made to prepare nanoparticles of transition metal phosphides, and the most promising results were obtained with the solution-phase high-temperature decomposition of organometallic molecular precursors, which yielded spherical, rod-like and hyperbranched cobalt, nickel, iron, vanadium, and manganese phosphide nanoparticles,[7−15] while Cu_3P nanoparticles had been prepared almost exclusively by ball milling,[2] ceramic,[2,16] and solid−vapor[17] or solvothermal approaches.[18−22] Cu_3P is interesting as it could represent an air-stable and an environmentally friendly material in light and high capacity anodes since it has theoretical gravimetric capacities which are slightly higher than those of graphite but volumetric capacities more than three times larger than graphite (3020 $mAhcm^{-3}$ for Cu_3P and 830 $mAhcm^{-3}$ for graphite).[23,24]

In 2007, an alternative method for the synthesis of metal phosphide nanoparticles was reported by the groups of Schaak and Chiang[25,26] and consisted of a sequence of reactions in which, first, metallic nanoparticles were formed and, later, they were phosphorized with alkyl phosphines. The method was initially tuned for Ni_2P nanoparticles and later generalized to other transition metals, thus becoming the first valuable approach for the preparation of size-controlled and soluble Cu_3P particles in the nanosize regime.[27] The metallic nanoparticles obtained in the first step retained their size and shape upon phosphorization, and hence a good control over the metal growth guaranteed narrow size distributions of the corresponding phosphide nanocrystals. Often the phosphorization process has been found to proceed *via* the Kirkendall effect,[28,29] by which large enough metal nanoparticles lead to hollow

* Address correspondence to andrea.falqui@iit.it, albert.figuerola@qi.ub.es.

Received for review May 4, 2011 and accepted December 3, 2011.

Published online December 03, 2011
10.1021/nn203702r

structures, while slight modifications of this procedure yield "non-hollow" phosphide nanoparticles.[26]

Here we report two "one-pot" approaches for the preparation of colloidal Cu_3P nanocrystals, one of which is also capable of yielding Janus-like Cu−Cu_3P nanoparticles. In the first approach (Scheme 1a), Cu_3P nanocrystals with hexagonal plate-like shape and sizes tunable from 5 to 50 nm were synthesized *via* a direct, homogeneous nucleation of small Cu_3P nuclei, which could be grown bigger with longer reaction time. In the second approach (Scheme 1b), Cu_3P nanocrystals were obtained still using a one-pot synthesis in which first Cu nanocrystals were first formed, then phosphorized over time to Cu_3P. In this case, the formation of hollow nanostructures was never observed,[1,26] while instead we always found dimeric Janus-like nanoparticles as intermediates, with one domain made of Cu and the other made of Cu_3P, the two domains sharing a flat epitaxial interface. In this case, the intermediate Cu_3P domains in the Janus-like nanoparticles and the final Cu_3P nanocrystals exhibited a truncated hexagonal bipyramidal habit. If annealed at high temperature and under high vacuum, the Janus-like nanoparticles were dephosphorized, and thus transformed back to single nanocrystals of metallic copper. Such feature suggests a possible use of these nanoparticles as phosphorus sources.

We studied the electrochemical lithiation of both the Cu_3P nanoplates and the Cu−Cu_3P Janus-like particles and found that the lithium ions can be reversibly intruded and extruded from the phosphide nanoplates, following a reversible displacement reaction (between lithium and copper ions) that makes them an attractive material for applications in lithium ion batteries. On the other hand, the electrochemical properties displayed by the Janus-like nanoparticles with respect to lithiation were remarkably different, due to the presence of large copper domains.

RESULTS AND DISCUSSION

In both synthesis approaches that we followed, a mixture of 3 g of trioctylphosphine oxide (TOPO) and the desired amount of trioctylphosphine (TOP) was degassed in a reaction flask for 2 h at 150 °C under vacuum and then put under inert atmosphere at 370 °C. In a second flask, a solution of CuCl (0.4 mmol), oleylamine (2.4 mmol), and octylamine (2.4 mmol) was prepared under inert atmosphere and then heated at 180 °C for 2 h to get a clear solution, after which it was cooled to 150 °C and its content was rapidly injected *via* a syringe into the first reaction flask. The resulting mixture was kept at 350 °C for the desired time and then cooled to room temperature.

In the syntheses, the relative amounts of TOP and CuCl dictated whether direct nucleation of Cu_3P nanocrystals occurred, followed by their growth (first approach), or alternatively, first Cu nanocrystals were formed and then converted into Cu_3P (second approach). Direct nucleation of Cu_3P nanocrystals, with no apparent intermediate formation of Cu nanocrystals, was observed when 2 mL (1.66 g) of TOP or more was added, which corresponds to a TOP:Cu molar ratio of at least 11:1. A typical time evolution of the Cu_3P nanoparticles is displayed in Figure 1a−d, which reports transmission electron microscopy (TEM) images of aliquots taken at

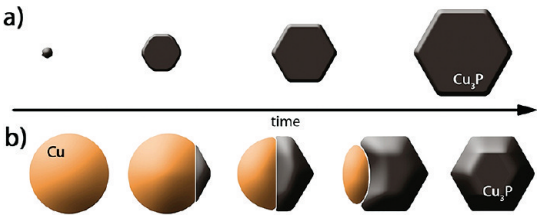

Scheme 1. Sketches of the two synthesis approaches to Cu_3P nanocrystals. Approach (a) is based on the direct, homogeneous nucleation of platelet-shaped Cu_3P nanocrystals, which then grow over time. In approach (b), first Cu nanoparticles are grown, and then they are progressively phosphorized to Cu_3P Janus-like particles in which the volume fraction of the truncated bipiramidal Cu_3P domain increases over time.

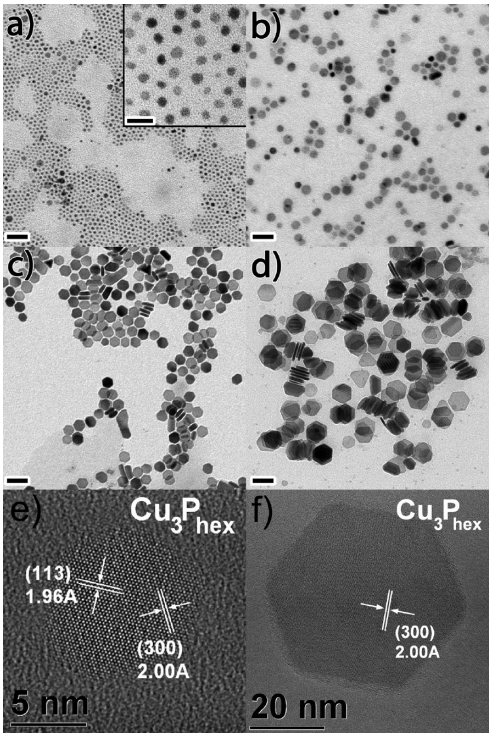

Figure 1. TEM images documenting the direct formation of Cu_3P nanoplates in solution when working at a TOP:Cu molar ratio of 11:1. Images refer to aliquots recovered after (a) 10 s, (b) 2 min, (c) 15 min, and (d) 25 min of reaction. The scale bar is 50 nm for the panels and 20 nm for the inset. (e,f) HRTEM images of Cu_3P nanoplates after 10 s and 25 min of reaction, respectively. In both cases, the nanocrystals show a structure clearly ascribable to the hexagonal Cu_3P phase.

different times. Small Cu_3P nuclei, with sizes around ~5 nm and hexagonal shape, were observed already a few seconds after injection (Figure 1a). After 2 min (Figure 1b), nanocrystals with hexagonal plate-like morphology were observed, and the morphology was retained for longer reaction times (Figure 1c,d), during which the nanocrystals became bigger (they typically reached 50 nm after 30 min). Therefore, the final size of these plate-like nanocrystals could be easily controlled by the total reaction time.

When the amount of TOP was increased from 2 mL to 3 and 4 mL, a faster nucleation and growth occurred. After less than 1 min of reaction, a polydisperse product in which many particles were already 50 nm big was observed. These observations could suggest that after an initial short burst of nucleation, and once the concentration of monomers is below the nucleation threshold, the further growth of Cu_3P nanocrystals probably proceeds *via* diffusion of monomer species following the Ostwald ripening mechanism:[30−32] small particles will gradually dissolve to form new monomer species that will diffuse to the surface of the largest nanocrystals, thus increasing the size of the latter. In agreement with this mechanism, the polydispersity of the Cu_3P samples has been observed to increase with the average crystal size: a defocusing ripening characteristic of the Ostwald ripening mechanism is enhanced upon increasing the TOP amount. Variations in the amount of TOPO instead did not have a major effect on the nucleation and growth rates, suggesting that TOPO behaved more like a solvent, while TOP was the main source of phosphorus. This is in agreement with the observations of Tracy and co-workers for Ni_2P nanocrystals.[30] The nanocrystals had Cu_3P hexagonal structure (space group $P6_3cm$), as confirmed by high-resolution TEM (HRTEM, Figure 1e,f) and XRD pattern, reported in Figure S1d (Supporting Information). These nanoplates tended to form columnar stacks on the carbon support film upon evaporation of the solvent (Figures 1d and S1a−c), as previously found by various groups on disk-like particles of other materials.[33,34]

When instead a volume of TOP of less than 2 mL was used (for example, 1 mL, corresponding to a TOP:Cu ratio of 5.6:1), first Cu nanoparticles were formed, most likely due to a reduction of Cu^+ by the alkylamines present. Over time, these Cu particles reacted with TOP and were slowly converted to Cu_3P. A typical time evolution of the synthesis is reported in Figure 2, which displays TEM images of aliquots taken at 4, 10, 25, and 45 min of reaction time (*i.e.*, after the injection). At 10 and 25 min, particles composed of two domains of different electron contrast were clearly discerned. Especially in the aliquot at 25 min, each Janus-like particle was formed by one hemispherical domain and one faceted domain. In the aliquot at 45 min, only faceted particles were found. The XRD pattern of these Janus-like particles evidenced peaks arising from both

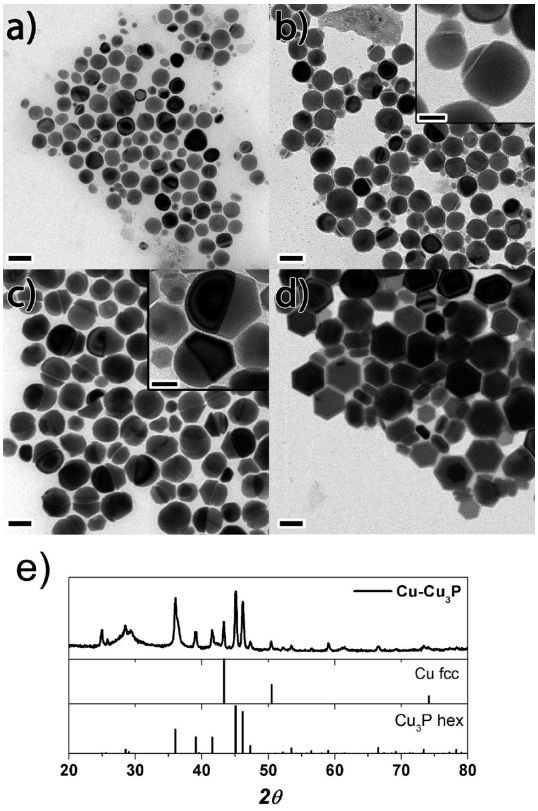

Figure 2. (a−d) TEM images documenting the formation of Cu nanoparticles and their progressive phosphorization when working at a TOP:Cu molar ratio of 5.6:1. Aliquots were collected at the following reaction times: (a) 4 min, (b) 10 min, (c) 25 min, (d) 45 min. The scale bar is 50 nm for the panels and 20 nm for the insets. (e) XRD pattern of the powder sample of Janus-like particles shown in panel c. Bulk reflexes of Cu and Cu_3P are also displayed. As a note, also in this second reaction mechanism, the relative amount of TOPO (ranging from 2 to 4 g) did not have any effect on the chemical conversion of Cu into Cu_3P, which confirms the role of TOP as the phosphorus precursor.

metallic Cu and Cu_3P (Figure 2e), as indexed according to the JSPDS card Nos. 03-1018 and 71-2261, respectively. Previous works by Wang *et al.* and Muthuswamy *et al.* have already reported the importance of the TOP/metal ratio for the preparation of the stoichiometric phosphide in the case of Ni_2P.[35,36] In those cases, high TOP/Ni ratios were required for the formation of solid Ni_2P or mixtures of P-rich Ni_xP_y phases, similar to our observations in the direct growth of Cu_3P plate nanocrystals. Oppositely, when using low TOP/Ni ratios, the authors of both works observed the formation of metallic Ni nanoparticles in a first step, in agreement with our experiments under similar TOP/Cu ratios that led to crystalline Cu nanocrystals. However, both authors report on the transformation of such Ni nanoparticles into hollow Ni_2P nanocrystals upon thermal annealing in solution. The Kirkendall effect was responsible for this transformation, during which the outward Ni diffusion rate was faster than the inward P diffusion rate with respect to the core of the metallic particle. This phosphorization mechanism generally leads to

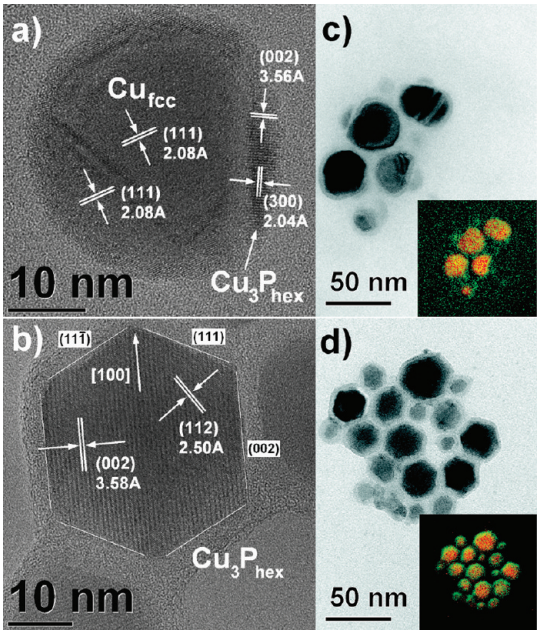

Figure 3. HRTEM and EFTEM images displaying the evolution of Cu−Cu_3P nanocrystals obtained by phosphorization of the Cu nanoparticles after (a,c) 10 min and (b,d) 45 min of reaction. (a,b) HRTEM images of a particle representative of each sample. (c,d) EFTEM zero-loss images of the two samples, with their inset showing P (green) and Cu (red) EFTEM maps of the same zones.

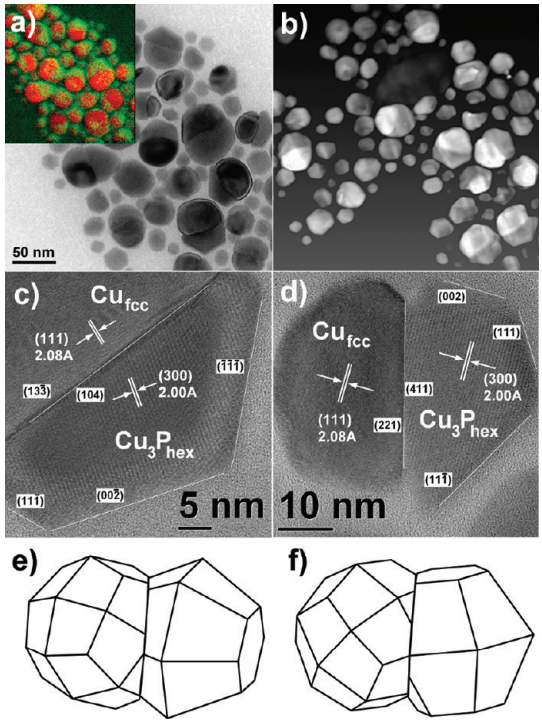

Figure 4. Evolution of the initial copper nanocrystals after 25 min of phosphorization, leading to the formation of Janus-like Cu−Cu_3P heterostructures. (a) EFTEM zero-loss images of the sample, with inset showing P (green) and Cu (red) EFTEM maps of the same zone. (b) Three-dimensional volume reconstruction and (c,d) HRTEM images of the dimers. The lighter part of each dimer is the one constituted by copper. The Cu and Cu_3P domains are attached following two types of epitaxial relationships: (c) $Cu_3P(411)//Cu(221)$ together with $Cu_3P\langle 0\bar{1}1\rangle//Cu\langle\bar{1}10\rangle$ and (d) $Cu_3P(104)//Cu(13\bar{3})$ together with $Cu_3P\langle 0\bar{1}0\rangle//Cu\langle\bar{3}21\rangle$ (interface and vector alignment relationship, respectively). (e,f) Reconstruction of the crystalline shape of the structures shown in (c) and (d), respectively.

centrosymmetric hollow structures like the ones reported by the works of Wang *et al.* and Muthuswamy *et al*. On the contrary, in the case of our Cu_3P nanocrystals obtained through the phosphorization process of initial metallic Cu particles, the Kirkendall effect has never been observed to take place. Alternatively, an epitaxial phosphorization process has been observed, as will be described later, which led to Janus-like particles instead of hollow nanostructures.

HRTEM analysis (Figure 3a) confirmed that in the Janus-like particles the spherical domain was Cu, with face-centered cubic (fcc) crystalline structure (space group *Fm*3*m*), while the faceted domain was Cu_3P, with crystal lattice ascribable to *hexagonal* Cu_3P. HRTEM analysis (Figure 3b) on the particles recovered at later times indicated instead that they were Cu_3P nanocrystals, with no more Cu domains attached to them. Within the intrinsic limitations of the Energy Filtered TEM (EFTEM) reported in literature,[37,38] the EFTEM images (insets of Figure 3c,d) mapped the spatial distribution of copper (red) and phosphorus (green) in these two samples, in agreement with the structural identification of the domains composing the nanostructures provided by HRTEM.

These morphologies suggest that the phosphorization most likely proceeds *via* the nucleation of a small Cu_3P domain only on one site on the surface of the initial Cu nanocrystals, which then extends progressively from that region to the whole nanocrystal. Kinetic factors, such as an inhomogeneous coverage of the particle surface by the surfactants, could be responsible for that. If all facets of Cu nanocrystals were equally available to the P precursor, the phosphorization reaction would probably proceed in a centrosymmetric way, leading to a Cu@Cu_3P core−shell morphology. If instead certain facets are more exposed to the reaction medium than others, the phosphorization will initiate more easily from there, and Janus-like particles will be formed, like the ones observed here. However, thermodynamic reasons cannot be ruled out, as, for instance, the presence of certain epitaxial interfaces between the Cu and Cu_3P domains that would minimize the energy and would then become preferential (the structural characterization of the observed epitaxial interfaces is discussed later). Hence, as soon as an active site is found for TOP to react on the surface of a Cu nanocrystal, further phosphorization will proceed only from that site. Also, it is remarkable that in the present phosphorization scheme of a Cu nanocrystal there appears to be no large unbalance in the relative diffusion rates of Cu and P species, which would have yielded hollow Cu_3P structures if, for example, P were diffusing much slower than Cu species.[29]

To better understand the mechanism leading to the formation of the Cu_3P nanocrystals obtained by progressive phosphorization of Cu nanoparticles, an in-depth TEM analysis of the intermediate steps of reaction was carried out. Figure 4 displays the results of this analysis, including HRTEM, EFTEM, and electron tomography (ET). The latter was performed using high-angular annular dark field (HAADF) imaging in scanning TEM (STEM): as in this mode the intensity depends on Z^2, the STEM-HAADF is very effective in distinguishing materials with different mean atomic number. In particular, Figure 4b displays the 3D volume reconstruction of the dimeric Janus-like heterostructures as obtained by ET analysis, where the lighter part of each Janus particle is that made of metal copper. A short movie showing the space rotation of the sample shown in Figure 4b is reported as part of the Supporting Information.

Moreover, *via* a detailed analysis of HRTEM[39,40] (see Figure 4c,d) data of several Cu−Cu_3P heterostructures, we identified two distinct epitaxial growth processes of Cu_3P on Cu occurring during the phosphorization of the Cu nanocrystals. In both cases, the $Cu_3P(300)$ lattice planes were found aligned with the Cu(111) lattice planes along the epitaxial interfaces according to the following crystallographic relationships:

$$Cu_3P(411)//Cu(221) \text{ and } Cu_3P\langle 0\bar{1}1\rangle//Cu\langle \bar{1}10\rangle \quad (1)$$

$$Cu_3P(104)//Cu(13\bar{3}) \text{ and } Cu_3P\langle 0\bar{1}0\rangle//Cu\langle \bar{3}21\rangle \quad (2)$$

where the left terms represent the interface alignment and the right terms represent the vector alignment. In particular, for the former epitaxial rule, the angular mismatch between the $Cu_3P(300)$ and Cu(111) lattice planes was 11°, whereas for the latter, the $Cu_3P(300)$ and Cu(111) lattice planes were perfectly parallel. For each epitaxial relationship, the lattice mismatch was calculated considering the projections of the main lattice planes $Cu_3P(300)$ and Cu(111) onto the corresponding epitaxial interfaces. We can define the lattice mismatch (m) between two lattice sets along a certain direction as follows:

$$m = | d_1 - d_2 | / 0.5(d_1 + d_2) \times 100\%$$

In the expression above, d_1 and d_2 represent the projected lengths of $Cu_3P(300)$ and Cu(111) lattice planes onto their corresponding epitaxial interfaces; m was calculated to be 0.9 and 0.5% for the epitaxial relationships 1 and 2 reported above, respectively, which indicates a good fit of the two crystalline domains composing the Cu−Cu_3P heterostructures that have commensurate misfit along the epitaxial interfaces. By combining HRTEM and 3D volume reconstruction resulting from electron tomography analysis, we could determine both the epitaxial relationships between the two domains composing the heterostructures and their crystalline habit as displayed in Figure 4e,f, where we reported the sketches of the nanocrystals imaged in Figure 4c,d, respectively. When the reaction was carried out until complete phosphorization, the final Cu_3P nanocrystals had truncated hexagonal bipyramid habit, which is different from the plate-like habit of the nanocrystals synthesized by direct nucleation of Cu_3P. This can be further observed in the short movie showing the space rotation of the same zone imaged in Figure S2 and reported as part of Supporting Information.

The Cu−Cu_3P eutectic in the Cu−P bulk alloy is well-known in metallurgy and has been studied extensively in the past,[41] and it is interesting to recall that in 1988 Selke *et al.*[42] rapidly cooled bulk Cu−P alloys at 15% P, close to the Cu−Cu_3P eutectic point (15.7% P), and found a microcrystalline lamellar structure of alternating Cu and Cu_3P layers with preferential orientation. The lamellae were stacked according to the planar orientation relationship $Cu_3P(010)//Cu(111)$ and with epitaxial interface parallel to Cu(111) and $Cu_3P(010)$ lattice planes. These relationships, which according to the authors should minimize the interfacial energy, are different however from those we found in the Janus-like Cu−Cu_3P nanocrystals. We observed instead a perfect parallelism between the $Cu_3P(300)$ and Cu(111) lattice planes for one orientation relationship but not for the second one, where the $Cu_3P(300)$ and Cu(111) lattice planes are slightly misaligned. Besides, the epitaxial interfaces in our Cu−Cu_3P dimeric heterostructures were tilted with respect to the $Cu_3P(300)$ and Cu(111)lattice sets, and this was observed for both 1 and 2 (see above) orientation relationships, which is clearly different from the quenched Cu−P alloys.

The above differences can be rationalized in terms of the remarkably different conditions in which the two types of heterostructures were prepared. The formation of a eutectic requires the initial melting of the components and the subsequent solidification of the alloy below the eutectic temperature, which in the specific case of the Cu−P system is 714 °C. It is well-known that nanoparticles have in general lower melting temperatures, compared to those of the corresponding materials in their bulk form. However, even if it is very likely that the nanoparticles have eutectic temperature lower than 714 °C, we can assume that such a temperature should be still higher than the maximum one (370 °C) involved in our nanocrystal syntheses. Moreover, rapid cooling of the Cu−Cu_3P eutectic by Selke *et al.* led to a spinodal decomposition process, with possible volume constraints in the evolution of the lamellar phase, which could have imposed the kinetically driven formation of only specific sets of interfaces. In our case, the phosphorization of Cu particles occurred in the solution phase; therefore, the nucleation and growth of Cu_3P crystals most likely proceeded without volume constraints, so that their

growth was favored along those crystallographic directions that minimized the most the interfacial energies, as suggested by the reported low mismatch values measured in the Cu−Cu_3P nanocrystals.

One aspect that Cu−Cu_3P eutectic in the bulk alloy and our nanoparticles certainly have in common is the evolution of extended and flat interfaces between the Cu and Cu_3P domains. This indicates that, despite the markedly different experimental conditions, in the Cu−Cu_3P system there is preference for development of specific sets of low-energy interfaces over ill-defined, defective interfaces. This concept, if extended to other alloy/eutectic systems that exhibit similar behavior, might help to predict the formation of nanoscale heterostructures with flat, epitaxial interface between domains of two different materials.

In order to investigate the thermal stability of the Janus-like particles, a HRTEM *in situ* annealing study was performed on the Janus-like Cu−Cu_3P particles drop-cast onto a MEMS microheater.[43] After annealing at temperatures between 400 and 500 °C, the Cu_3P domains were found to transform into Cu, as shown in Figure 5a,b, so that homogeneous, single-crystalline Cu particles were obtained, due to a dephosphorization caused by the evaporation of P into the vacuum.

At all considered temperatures, the Cu particles were still crystalline and no melting was observed. The smaller Janus-like particles were found to dephosphorize at lower temperatures and after shorter time durations than larger particles. After heating at a temperature of 500 °C for 60 min, any remaining Janus-like particles (with Cu_3P domains) were typically those larger than 15 nm. When the samples were heated between 100 and 200 °C, a number of Janus-like particles exhibited a peculiar behavior: in Cu_3P domain, a pattern of atomic columns was visible which did not correspond to Cu, neither to the hexagonal Cu_3P structure, as displayed in the HRTEM image reported in Figure 5c. Instead, it showed a typical [110] projection of a fcc-type structure. When assuming that the Cu_3P variant is cubic, the lattice parameter for fcc-type copper phosphide (Cu_3P_{fcc}) can be estimated at 4.16 Å. Besides, from Figure 5c, the following orientation relationship could be deduced:

$$Cu_3P_{1-xfcc}\{100\}//Cu\{1\bar{1}0\} \text{ and}$$
$$Cu_xP_{1-xfcc}[011]//Cu[11\bar{2}]$$

The planar alignment coincides with the orientation of the interface, so that Cu_3P_{1-xfcc}[100]//Cu [$1\bar{1}0$] are vectors normal to the interface, while Cu_3P_{1-xfcc}[011]// Cu [$11\bar{2}$] are vectors parallel to the interface. These findings indicate that the starting hexagonal crystalline structure of the Cu_3P domain changed into a fcc one, being the main advantage of the presence of such a new stacking that it creates a fcc-type $Cu_3P_{1-x}\{022\}$ spacing of 1.47 Å in the plane of the interface: this is

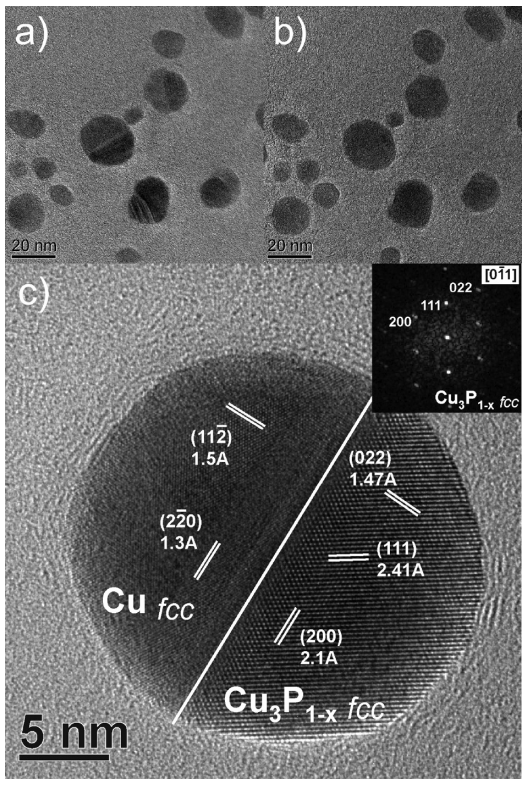

Figure 5. Evolution of the Janus-like Cu−Cu_3P nanocrystals due to *in situ* thermal annealing under vacuum, as performed in the HRTEM. (a) Particles imaged at 450 °C, where the dark domains are made of Cu and the lighter ones are made of Cu_3P; (b) same particles shown in (a), but after annealing at 500 °C for 10 min: the particles are single-crystalline and with the fcc copper structure. (c) Janus-like particle after annealing at 150 °C. The Cu_3P domain appears to have a fcc-type crystalline structure oriented along the [110] zone axis, with lattice parameter equal to 4.16 Å. The copper domain is oriented along the [111] zone axis.

compatible with the Cu{112} lattice spacing of 1.48 Å, and the cubic Cu_3P_{1-x} phase therefore fits much better onto the Cu lattice. This structural change is most likely associated with a variation of the Cu/P stoichiometry. Interestingly, similar behavior was not observed in the Cu_3P nanoplates that, even if heated at 550 °C for more than 30 min, did not dephosphorize. Due to this experimental evidence, further investigations on the formation and evolution of such a new Cu_3P_{1-x} phase will be subject of a dedicated paper.

One possible application of the nanoparticles developed in the present work is in lithium ion batteries, as already pointed out in the introduction for this class of materials. To this aim, we investigated the electrochemical properties of the Cu_3P nanoparticles prepared following the first synthetic approach, which yielded plate-like morphology. Cyclic voltammetry (CV) and electrochemical impedance spectroscopy (EIS) were employed to probe the lithiation and delithiation behavior of the platelets. It is well-known from previous works that the lithiation process on Cu_3P electrodes leads to the formation of metallic copper upon a

progressive displacement with Li^+ ions, and upon delithiation, the extruded copper is reincorporated so that the Cu_3P phase is recovered. The process can be represented as[44,45]

$$Cu_xP + xLi \Leftrightarrow Li_xCu_{x-1}P + Cu^0$$

This quasi-reversible displacement reaction has manifested in a reversible capacity around 370−380 mAh/g for Cu_3P based nanostructures and thick films reported so far.[17,46] In our case, the Cu_3P nanoplates could easily be indentified in the random dispersions from the sampled composite (85 wt %) used for preparing the electrodes, due to the fact that their plate-like morphology remained intact (see Figure 6b). After the first discharge from 3.0 to 0.02 V on galvanostatic mode, the charge cycle was followed by the impedance analysis in order to understand the processes at the electrode, as reported in Figure 6a. The cells were charged to different potentials, and the electrode impedance was measured. The resulting semicircles (inset of Figure 6a) in the high-frequency region could be ascribed to the occurrence of the charge-transfer process (due to the transfer of Li^+ ions) through the electrode/electrolyte interface and the presence of the solid electrolyte interface (SEI), followed by the spike-like region at 45° in the lower frequency region of impedance spectra that shows a solid-state Li^+ ion diffusion in the electrode. At OCPs (open circuit potential) below 1 V, the electrodes had pronounced semicircles that were greatly enlarged upon delithiation as for Cu_3P at higher potentials. In agreement with previous literature reports,[17,44−46] at reduction potentials below 1.0 V, the progressively extruded Cu ions appeared to be crystallized into metal domains, while upon Cu intrusion, the initial Cu_3P phase was recovered. This seemed to occur at oxidation potentials starting from 1.0 to 2.4 V (see Figure 6a). This reversibility of Cu metal extrusion/intrusion upon charge/discharge indicated that hexagonally close-packed lattice of Cu_3P nanoplates has the capability to withstand the possible structural deformation caused during cycles by the intrusion/extrusion of both Cu and Li ions. Cyclic voltammograms (CVs), as reported in Figure 6c, further illustrated the complex nature of lithiation/delithiation processes which proceed through multiple steps on the Cu_3P nanoplates. From the CVs, the Cu displacement reaction with Li^+ ions started from about 1.5 V *versus* Li and continued when moving toward more negative potentials. There were several peaks (indicating lithiation in different steps) further in the cathodic scan followed by a strong reduction peak centered at 0.4−0.3 V during the first CV cycle (as reported in the inset), where most of the Cu ions had been extruded from the hexagonal crystal lattice as they were replaced by Li^+ ions. At 0.02 V, about 3.5 Li^+ ions per Cu_3P would be required to

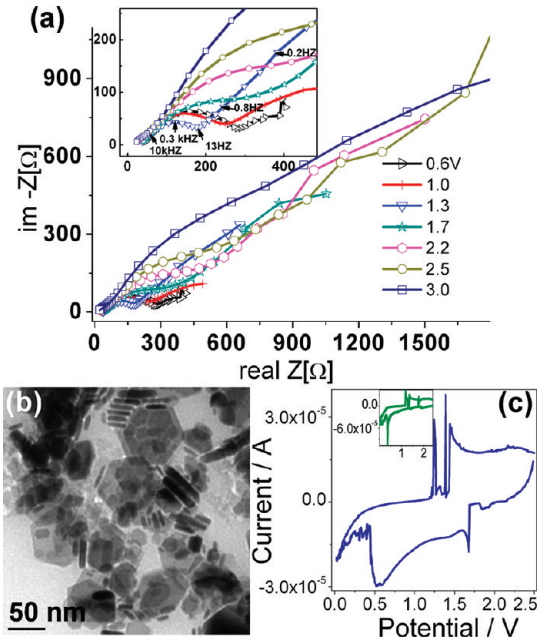

Figure 6. (a) Impedance spectra of the Cu_3P electrode as the function of open circuit potential (OCP); the inset is a magnification of the high-frequency region. (b) Cu_3P nanoplates in the composite electrode. (c) Cyclic voltammogram (CV) of second cycle at 0.5 mV s^{-1}, illustrating the complex lithiation process involving the Cu_3P electrodes. The inset reports the CV of the first cycle.

complete the displacement reaction and to achieve complete reduction of copper to Cu^0 during the progressive lithiation. In the oxidation process, the sharp peaks at 1.1, 1.3, and 1.5 and a shoulder at 1.8 V were indicative of in-step Cu intrusion reaction to form Cu_3P. This is in good agreement with the impedance data on a charge cycle above 2.0 V, where the progressively enlarged semicircles indicate that the electrode resistance increased as in the case of Cu_3P. In the second cycle (Figure 6c), most of the peaks were retained and shifted slightly toward more positive potentials and slowly stabilized in the successive cycles.

We additionally characterized the electrochemical properties of the Janus-like Cu−Cu_3P nanoparticles. One motivation in this direction came from considerations that a battery performance depends also on the electronic conductivity of the electrodes and on the interface between the electrodes and the current collectors,[11] and that one way to optimize these features would be offered by hybrid nanocrystals in which the metallic domain would improve electronic conductance, as possibly in the case of the present Janus-like dimers. In other words, nanostructured electrodes where both an electroactive domain and a robust metallic nanodomain are homogeneously combined could be, in principle, ideal for effective and lasting lithium ion batteries. In this regard, a previous work on Cu_3P by Villevieille *et al.* reported substantial improvements in terms of cyclability when Cu_3P nanoparticles were grown on metallic Cu nanorods working

as current collectors, which was claimed to be due to both the nanometric dimensions of the materials and to the quality of the interface between them.[17] However, as reported in Figure S3 of the Supporting Information, the same CV analysis carried out on the Cu−Cu_3P nanoparticles was clearly indicative of irreversible electrochemical processes. Basically, a strong reduction current in the cathodic scan was observed, but on the oxidation process, almost no activity was measured. The impedance analysis of a typical electrode built from Cu−Cu_3P nanocrystals indicated that the resistance of the electrode increased irreversibly from the second cycle. We ascribed this behavior to the presence of the large metal copper domains, which most likely cause irreversible alloying processes.

CONCLUSIONS

In conclusion, we have reported here two "one-pot" approaches for the preparation of size-controlled Cu_3P nanoparticles within the 5−50 nm range. In the first approach, plate-like Cu_3P nanocrystals with hexagonal structure were directly nucleated and could be easily grown over time. Using this strategy, the usual procedures that involve the preparation of copper nanocrystals and their subsequent phosphorization could be avoided, and samples of nanostructured and size-controlled pure Cu_3P were obtained in a more reproducible fashion. The electrochemical properties suggested that the as-prepared Cu_3P nanoplates could be used as anode material in lithium ion batteries. The second approach is in reality a modification of the previous one and leads to the formation of Cu−Cu_3P Janus-like nanoparticles with interfaces that resemble those found in rapidly cooled Cu−Cu_3P eutectics. Annealing of these Janus-like particles at temperatures higher than 400 °C under vacuum starts a process of dephosphorization of the Cu_3P domain, which first undergoes an hexagonal → fcc structural change in the region at the interface with the Cu domain, and is finally converted back to Cu upon complete dephosphorization. Finally, an extensive characterization of both the Cu_3P nanoplates and the Janus particles was carried out, indicating that the Cu_3P nanoplates could represent an attractive material for applications in lithium ion batteries, due to their cyclability properties in the lithiation/delithiation process. On the contrary, the electrochemical behavior displayed by the Janus-like nanoparticles indicates that the presence of the larger copper domains makes them unsuitable for applications in batteries.

METHODS

All reactions were carried out under nitrogen using standard air-free techniques.

Chemicals. Copper chloride (CuCl, 99.999%), trioctylphospine oxide (TOPO, 99%), and tri-*n*-octylphosphine (TOP, min. 97%) were purchased from Strem Chemicals. Oleylamine (OLAM, 70%), octylamine (OCAM, 99%), and toluene anhydrous (99.8%) were purchased from Sigma-Aldrich. Ethanol absolute anhydrous was purchased from Carlo Erba reagents. Oleylamine was degassed using a standard Schlenk line under vacuum at 150 °C for 3 h and then stored in a glovebox under inert atmosphere. All of the other chemicals were used as received. Polypropylene microporous matrixes were purchased from Cellguard. Li metal foils were purchased from Goodfellow (UK). Lithium hexafluorophosphate (battery grade, ≥99.99%), ethylenecarbonate, diethylcarbonate, *N*-methyl-2-pyrrolidone, polyvinylidenedifluoride (PVDF), and carbon powder were purchased from Aldrich. All of the solvents used were degassed and handled in the glovebox.

Synthesis of Cu_3P Nanocrystals. A solution of CuCl (0.4 mmol), oleylamine (2.4 mmol), and octylamine (2.4 mmol) was prepared under inert atmosphere and then heated at 180 °C for 2 h to get a clear solution. A mixture of 3 g of TOPO and 2 mL of TOP (Cu:TOP ratio 1:11.2) was degassed in a reaction flask for 2 h at 150 °C under vacuum using a standard Schlenk line. The copper solution was then cooled to 150 °C and then rapidly injected into the reaction flask at 370 °C. The reaction was heated at 350 °C for the desired time and then slowly cooled to room temperature. In the standard washing procedure used, the crude reaction mixture is mixed with toluene and ethanol and centrifuged (3200 rpm) for 10 min. The precipitate was dispersed in 1 mL of toluene and sonicated for 5 min at 40 °C. After adding 5 mL of ethanol, the dispersion was centrifuged for 15 min at 3200 rpm. The cleaning procedure was repeated three more times to get a clean product that was finally redispersed in toluene and kept in a glovebox.

Phosphorization of Cu To Form Cu_3P. A solution of CuCl (0.4 mmol), oleylamine (2.4 mmol), and octylamine (2.4 mmol) was prepared under inert atmosphere and then heated at 180 °C for 2 h to get a clear solution. A mixture of 3 g of TOPO and 1 mL of TOP (Cu:TOP molar ratio 1:5.6) was degassed in a reaction flask for 2 h at 150 °C under vacuum using a standard Schlenk line. The copper solution was then cooled to 150 °C and then rapidly injected into the reaction flask at 370 °C. The reaction was heated at 350 °C for the desired time and then slowly cooled to room temperature. To clean the product the same washing procedure described above was used.

Electron Microscopy Characterization. Morphological, structural, and compositional analyses were carried out by conventional transmission electron microscopy (TEM), electron tomography (ET) in scanning TEM (STEM), high-resolution TEM (HRTEM), and energy filtered TEM (EFTEM) measurements. TEM images were recorded on a JEOL JEM 1011 microscope, equipped with a W electron source and operating at an acceleration voltage of 100 kV. Electron tomography in scanning TEM (STEM) working in high-angle annular dark field (HAADF) mode, high-resolution TEM (HRTEM), and energy filtered (EFTEM) measurements were performed on a JEOL JEM-2200FS microscope, equipped with a field emission gun (FEG) working at an accelerating voltage of 200 kV, an objective lens (OL) CEOS spherical aberration corrector, an Omega energy filter. Energy filtered images were acquired using a contrast aperture of about 10 mrad to reduce aberrations (mostly chromatic). Chemical maps from P K (2146 eV) and Cu L (931 eV) edges were obtained by acquiring three images (one post-edge and two pre-edge), respectively, to extract the background, with an energy slit of 60 eV for P and 40 eV for Cu. The reconstruction of the 3D shape of the samples was performed by using the SIRT algorithm with 40 iterations. The *in situ* annealing HRTEM analysis was performed on a cubed FEI Titan microscope, equipped with a FEG gun, an OL CEOS spherical aberration corrector and working at an acceleration voltage of 300 kV. The *in situ* annealing HRTEM experiments were performed on a thermal range from room temperature to 600 °C by a microelectronic mechanical system (MEMS) microheater-based low-drift sample holder whose description is reported in detail in ref 36. The samples for TEM analysis were

prepared in a glovebox by depositing a few drops of a dilute solution of nanocrystals onto carbon-coated Cu grids. The latter were then transferred immediately into the microscope.

X-ray Powder Diffraction (XRD). XRD measurements were performed with a Rigaku SmartLab X-ray diffractometer. Concentrated nanocrystal solutions were spread on top of a silicon substrate, after which the sample was allowed to dry and was then measured in parallel beam reflection geometry 2Θ/Θ using Cu Kα wavelength. For phase identification, we used PDXL software of Rigaku.

Electrochemical Characterization. All of the electrochemical measurements were carried out using a PARSTAT2273 potentiostat/galvanostat. The nanoparticles were washed several times with a mixture of toluene and ethanol and dried under N_2 for several hours. The electrodes were prepared by mixing the dried nanoparticles with PVDF (wt % 85 in nanoparticle) in *N*-methyl-2-pyrrolidone to form a homogeneous composite paste. The paste was then coated onto the current collectors and dried at 140 °C for several hours. Cell components for type 2032 button type were purchased from Hohsen Corporation (Jp); 2032 cells were assembled in an Ar-filled glovebox, using 85 wt % of the active material as working electrode and Li metal as both reference and counter electrode. A 1:1 mixture of ethylenecarbonate and diethylcarbonate containing lithium hexafluorophosphate served as electrolyte.

Acknowledgment. The authors acknowledge financial support from European Union through the FP7 starting ERC grant NANO-ARCH (Contract Number 240111). Zineb Saghi acknowledges financial support from the European Union under the Framework 6 program for an Integrated Infrastructure Initiative, Reference 026019 ESTEEM. Mauro Povia is acknowledged for help with the XRD measurements.

Supporting Information Available: Additional experimental details. This material is available free of charge *via* the Internet at http://pubs.acs.org.

REFERENCES AND NOTES

1. Brock, S. L.; Senevirathne, K. Recent Developments in Synthetic Approaches to Transition Metal Phosphide Nanoparticles for Magnetic and Catalytic Applications. *J. Solid State Chem.* **2008**, *181*, 1552–1559.
2. Bichat, M.-P.; Politova, T.; Pfeiffer, H.; Tancret, F.; Monconduit, L.; Pascal, J.-L.; Brousse, T.; Favier, F. Cu_3P as Anode Material for Lithium Ion Battery: Powder Morphology and Electrochemical Performances. *J. Power Sources* **2004**, *136*, 80–87.
3. Bruce, P. G.; Scrosati, B.; Tarascon, J. M. Nanomaterials for Rechargeable Lithium Batteries. *Angew. Chem., Int. Ed.* **2008**, *47*, 2930–2946.
4. Arico, A. S.; Bruce, P.; Scrosati, B.; Tarascon, J. M.; Van Schalkwijk, W. Nanostructured Materials for Advanced Energy Conversion and Storage Devices. *Nat. Mater.* **2005**, *4*, 366–377.
5. Cabana, J.; Monconduit, L.; Larcher, D.; Palacin, M. R. Beyond Intercalation-Based Li-Ion Batteries: The State of the Art and Challenges of Electrode Materials Reacting through Conversion Reactions. *Adv. Mater.* **2010**, *22*, E170–E192.
6. Bichat, M. P.; Gillot, F.; Monconduit, L.; Favier, F.; Morcrette, M.; Lemoigno, F.; Doublet, M. Redox-Induced Structural Change in Anode Materials Based on Tetrahedral $(MPn_4)^{x-}$ Transition Metal Pnictides. *Chem. Mater.* **2004**, *16*, 1002–1013.
7. Perera, S. C.; Fodor, P. S.; Tsoi, G. M.; Wenger, L. E.; Brock, S. L. Application of Desilylation Strategies to the Preparation of Transition Metal Pnictide Nanocrystals: The Case of FeP. *Chem. Mater.* **2003**, *15*, 4034–4038.
8. Perera, S. C.; Tsoi, G.; Wenger, L. E.; Brock, S. L. Synthesis of MnP Nanocrystals by Treatment of Metal Carbonyl Complexes with Phosphines: A New, Versatile Route to Nanoscale Transition Metal Phosphides. *J. Am. Chem. Soc.* **2003**, *125*, 13960–13961.
9. Koo, J. P. B.; Hwang, Y.; Bae, C.; An, K.; Park, J. G.; Park, H. M.; Hyeon, T. Novel Synthesis of Magnetic Fe_2P Nanorods from Thermal Decomposition of Continuously Delivered Precursors Using a Syringe Pump. *Angew. Chem., Int. Ed.* **2004**, *43*, 2282–2285.
10. Qian, C.; Kim, F.; Ma, L.; Tsui, F.; Yang, P. D.; Liu, J. Solution-Phase Synthesis of Single-Crystalline Iron Phosphide Nanorods/Nanowires. *J. Am. Chem. Soc.* **2004**, *126*, 1195–1198.
11. Park, J.; Koo, B.; Yoon, Y. K.; Hwang, Y.; Kang, M.; Park, J.-G.; Hyeon, T. Generalized Synthesis of Metal Phosphide Nanorods *via* Thermal Decomposition of Continuously Delivered Metal-Phosphine Complexes Using a Syringe Pump. *J. Am. Chem. Soc.* **2005**, *127*, 8433–8440.
12. Li, Y.; Malik, M. A.; O'Brien, P. Synthesis of Single-Crystalline CoP Nanowires by a One-Pot Metal-Organic Route. *J. Am. Chem. Soc.* **2005**, *127*, 16020–16021.
13. Senevirathne, K.; Burns, A. W.; Bussell, M. E.; Brock, S. L. Synthesis and Characterization of Discrete Nickel Phosphide Nanoparticles: Effect of Surface Ligation Chemistry on Catalytic Hydrodesulfurization of Thiophene. *Adv. Funct. Mater.* **2007**, *17*, 3933–3939.
14. Maneeprakorn, W.; Malik, M. A.; O'Brien, P. The Preparation of Cobalt Phosphide and Cobalt Chalcogenide (CoX, X = S, Se) Nanoparticles from Single Source Precursors. *J. Mater. Chem.* **2010**, *20*, 2329–2335.
15. Zhang, H.; Ha, D.-H.; Hovden, R.; Fitting Kourkoutis, L.; Robinson, R. D. Controlled Synthesis of Uniform Cobalt Phosphide Hyperbranched Nanocrystals Using Tri-*n*-octylphosphine Oxide as a Phosphorus Source. *Nano Lett.* **2011**, *11*, 188–197.
16. Pfeiffer, H.; Tancret, F.; Brousse, T. Synthesis, Characterization and Electrochemical Properties of Copper Phosphide (Cu_3P) Thick Films Prepared by Solid-State Reaction at Low Temperature: A Probable Anode for Lithium Ion Batteries. *Electrochim. Acta* **2005**, *50*, 4763–4770.
17. Villevieille, C.; Robert, F.; Taberna, P. L.; Bazin, L.; Simon, P.; Monconduit, L. The Good Reactivity of Lithium with Nanostructured Copper Phosphide. *J. Mater. Chem.* **2008**, *18*, 5956–5960.
18. Su, H. L.; Xie, Y.; Li, B.; Liu, X. M.; Qian, Y. T. A Simple, Convenient, Mild Solvothermal Route to Nanocrystalline Cu_3P and Ni_2P. *Solid State Ionics* **1999**, *122*, 157–160.
19. Xie, Y.; Su, H. L.; Qian, X. F.; Liu, X. M.; Qian, Y. T. A Mild One-Step Solvothermal Route to Metal Phosphides (Metal = Co, Ni, Cu). *J. Solid State Chem.* **2000**, *149*, 88–91.
20. Aitken, J. A.; Ganzha-Hazen, V.; Brock, S. L. Solvothermal Syntheses of Cu_3P *via* Reactions of Amorphous Red Phosphorus with a Variety of Copper Sources. *J. Solid State Chem.* **2005**, *178*, 970–975.
21. Wang, X.; Han, K.; Gao, Y.; Wan, F; Jiang, K. Fabrication of Novel Copper Phosphide (Cu_3P) Hollow Spheres by a Simple Solvothermal Method. *J. Cryst. Growth* **2007**, *307*, 126–130.
22. Liu, S.; Qian, Y.; Xu, L. Synthesis and Characterization of Hollow Spherical Copper Phosphide (Cu_3P) Nanopowders. *Solid State Commun.* **2009**, *149*, 438–440.
23. Wang, K.; Yang, J.; Xie, J. Y.; Wang, B. F.; Wen, Z. S. Electrochemical Reactions of Lithium with CuP_2 and $Li_{1.75}Cu_{1.25}P_2$ Synthesized by Ball Milling. *Electrochem. Commun.* **2003**, *5*, 480–483.
24. Bichat, M. P.; Politova, T.; Pascal, J. L.; Favier, F.; Monconduit, L. Electrochemical Reactivity of Cu_3P with Lithium. *J. Electrochem. Soc.* **2004**, *12*, A2074–A2081.
25. Henkes, A. E.; Vasquez, Y.; Schaak, R. E. Converting Metals into Phosphides: A General Strategy for the Synthesis of Metal Phosphide Nanocrystals. *J. Am. Chem. Soc.* **2007**, *129*, 1896–1897.
26. Chiang, R.-K.; Chiang, R.-T. Formation of Hollow Ni_2P Nanoparticles Based on the Nanoscale Kirkendall Effect. *Inorg. Chem.* **2007**, *46*, 369–371.
27. Henkes, A. E.; Schaak, R. E. Trioctylphosphine: A General Phosphorus Source for the Low-Temperature Conversion of Metals into Metal Phosphides. *Chem. Mater.* **2007**, *19*, 4234–4242.
28. Fan, H. J.; Gösele, U.; Zacharias, M. Formation of Nanotubes and Hollow Nanoparticles Based on Kirkendall and Diffusion Processes: A Review. *Small* **2007**, *3*, 1660–1671.

29. Yin, Y.; Rioux, R. M.; Erdonmez, C. K.; Hughes, S.; Somorjai, G. A.; Alivisatos, A. P. Formation of Hollow Nanocrystals through the Nanoscale Kirkendall Effect. *Science* **2004**, *304*, 711–714.
30. Ostwald, W. Z. *Z. Phys. Chem.* **1901**, *37*, 385.
31. Lifshitz, I. M.; Slyozov, V. V. The Kinetics of Precipitation from Supersaturated Solid Solutions. *J. Phys. Chem. Solids* **1961**, *19*, 35–50.
32. Wagner, C. Z. Theorie der Alterung von Niederschlagen durch Umlosen (Ostwald-Reifung). *Elektrochem.* **1961**, *65*, 581–591.
33. Saunders, A. E.; Ghezelbash, A.; Smilgies, D. M.; Sigman, M. B.; Korgel, B. A. Columnar Self-Assembly of Colloidal Nanoplates. *Nano Lett.* **2006**, *6*, 2959–2963.
34. Li, X.; Shen, H.; Niu, J.; Li, S.; Zhang, Y.; Wang, H.; Li, L. S. Columnar Self-Assembly of Cu_2S Hexagonal Nanoplates Induced by Tin(IV)-X Complex as Inorganic Surface Ligand. *J. Am. Chem. Soc.* **2010**, *132*, 12778–12779.
35. Wang, J.; Johnston-Peck, A. C.; Tracy, J. B. Nickel Phosphide Nanoparticles with Hollow, Solid, and Amorphous Structures. *Chem. Mater.* **2009**, *21*, 4462–4467.
36. Muthuswamy, E.; Savithra, G. H. L.; Brock, S. L. Synthetic Levers Enabling Independent Control of Phase, Size, and Morphology in Nickel Phosphide Nanoparticles. *ACS Nano* **2011**, *5*, 2402–2411.
37. Lozano-Perez, S.; Titchmarsh, J. M. EFTEM Assistant: A Tool To Understand the Limitations of EFTEM. *Ultramicroscopy* **2007**, *107*, 313–321.
38. Verbeeck, J.; Bertoni, G. Model-Based Quantification of EELS Spectra: Treating the Effect of Correlated Noise. *Ultramicroscopy* **2008**, *108*, 74–83.
39. Deka, S.; Falqui, A.; Bertoni, G.; Sangregorio, C.; Poneti, G.; Morello, G.; De Giorgi, M.; Giannini, C.; Cingolani, R.; Manna, L.; *et al.* Fluorescent Asymmetrically Cobalt-Tipped CdSe@CdS Core@Shell Nanorod Heterostructures Exhibiting Room-Temperature Ferromagnetic Behavior. *J. Am. Chem. Soc.* **2009**, *131*, 12817–12828.
40. Maynadié, J.; Salant, A.; Falqui, A.; Respaud, M.; Shaviv, E.; Banin, U.; Soulantica, K.; Chaudret, B. Cobalt Growth on the Tips of CdSe Nanorods. *Angew. Chem., Int. Ed.* **2009**, *48*, 1814–1817.
41. Lindlief, W. E. Melting Points of Some Binary and Ternary Copper-Rich Alloys Containing Phosphorus. *Met. Alloys* **1933**, *4*, 85–88.
42. Selke, H.; Ryder, P. L. Microstructure and Crystallography of a Rapidly Quenched Eutectic Cu-P Alloy. *Acta Metall.* **1988**, *36*, 2387–2392.
43. Van Huis, M. A.; Young, N. P.; Pandraud, G.; Creemer, J. F.; Vanmaekelbergh, D.; Kirkland, A. I.; Zandbergen, H. W. Atomic Imaging of Phase Transitions and Morphology Transformations in Nanocrystals. *Adv. Mater.* **2009**, *21*, 4992–4995.
44. Crosnier, O.; Nazarz, L. F. Facile Reversible Displacement Reaction of Cu_3P with Lithium at Low Potential. *Electrochem. Solid-State Lett.* **2004**, *7*, A187–A189.
45. Pfeiffer, H.; Tancret, F.; Bichat, M. P.; Monconduit, L.; Favier, F.; Brousse, T. Air Stable Copper Phosphide (Cu_3P): A Possible Negative Electrode Material for Lithium Batteries. *Electrochem. Commun.* **2004**, *6*, 263–267.
46. Mauvernay, B.; Doublet, M. L.; Monconduit, L. Redox Mechanism in the Binary Transition Metal Phosphide Cu_3P. *J. Phys. Chem. Solids* **2006**, *67*, 1252–1257.